CORA Cork Open Research Archive
Cartlann Taighde Oscailte Chorcaí

Title	Hydrogenated silicon nanoclusters with a permanent electric dipole moment for the controlled assembly of silicon-based nanostructures
Authors	Jardali, Fatme;Keary, Bryan P.;Perrotin, Tatiana;Silva, François;Vanel, Jean-Charles;Bonnassieux, Yvan;Mazouffre, Stéphane;Ruth, Albert A.;Leulmi, Mohamed E.;Vach, Holger
Publication date	2021-11-16
Original Citation	Jardali, F., Keary, B. P., Perrotin, T., Silva, F., Vanel, J.-C., Bonnassieux, Y., Mazouffre, S., Ruth, A. A., Leulmi, M. E. and Vach, H. (2021) 'Hydrogenated silicon nanoclusters with a permanent electric dipole moment for the controlled assembly of silicon-based nanostructures', ACS Applied Nano Materials, 4(11), pp.12250-12260. https://doi.org/10.1021/acsanm.1c02754
Type of publication	Article (peer-reviewed)
Link to publisher's version	10.1021/acsanm.1c02754
Rights	© 2021, Association for Computing Machinery. This is the author's version of the work. It is posted here for your personal use. Not for redistribution. The definitive Version of Record was published in ACS Applied Nano Materials: https://doi.org/10.1021/acsanm.1c02754
Download date	2026-10-20 03:17:10
Item downloaded from	https://hdl.handle.net/10468/12268

UCC
University College Cork, Ireland
Coláiste na hOllscoile Corcaigh

Hydrogenated Silicon Nanoclusters with a Permanent Electric Dipole Moment for the Controlled Assembly of Silicon-Based Nanostructures

Fatme Jardali,[†] Bryan Patrick Keary,[‡] Tatiana Perrotin,[¶] François Silva,[†] Jean-Charles Vanel,[†] Yvan Bonnassieux,[†] Stéphane Mazouffre,[¶] Albert A. Ruth,[‡] Mohamed E. Leulmi,[§] and Holger Vach[*,†,‖]

†*LPICM, CNRS, Ecole Polytechnique, IP Paris, Palaiseau, France*

‡*Physics Department / Environmental Research Institute, University College Cork, Cork, Ireland*

¶*ICARE, CNRS, Orléans, France*

§*Center for SiNC Applications, Paris, France*

‖*Centre for Research in Molecular Modeling, Concordia University, Montreal, Canada*

E-mail: holger.vach@polytechnique.edu

Abstract

While silicon nanoclusters have extensively been used for their outstanding properties for many decades, never before their dipole moment has been exploited for any application. Here, we have succeeded in producing hydrogenated silicon nanoclusters with a strong permanent electric dipole moment. This dipole moment allows us to use electric fields in order to orient and guide individual clusters. As a first example, we

demonstrate the catalyst-free one-by-one self-assembly of one of the thinnest silicon nanowires yet observed. As a second example, we show that the simple presence of those nanoclusters on LaB_6 cathodes leads to a 30-fold enhancement of the thermionic electron current density over pristine LaB_6. Last but not least, the nanoclusters provide a protective layer against chemical and mechanical attack and largely prevent the evaporation of substrate materials potentially increasing the operational lifetime of cathodes substantially.

Keywords

hydrogenated silicon nanoclusters, thin silicon films, permanent electric dipole moment, self-assembled nano-structures, enhanced thermionic emission

1 Introduction

Silicon nanoclusters (SiNCs) and nanoparticles (SiNPs) have continuously attracted state-of-the-art research for several decades because of their interest for micro- and nanoelectronics.[1,2] Despite worldwide and intensive exploration, however, those nanoentities of silicon have not spoken their last word yet and keep on surprising when unveiling even more of their secrets. Some of the most recent research topics concern, for instance, hydrogen generation via mesoporous SiNP photocatalyse[3] and via oxidation of hydrogenated SiNCs;[4] therapeutic potentials of transferrin-functionalized porous SiNPs against glioma cell migration in brain tumor treatment;[5] facile procedure for the synthesis of ultra-fine SiNPs;[6] isolable unsaturated silicon clusters;[7–9] production of unoxidized, hydrogenated, and amorphous SiNPs using ultrasonic technologies;[10] improved understanding of interstellar dust grains, meteorites and asteroids;[11] functional nanophotonics;[12] exploration of unusual size dependence of electronic and optical absorption gaps of hydrogenated SiNPs;[13] and deposition of hydrogenated SiNCs for efficient epitaxial growth.[14]

While silicon nanoclusters have extensively been used for their outstanding properties for many decades, never before their dipole moment has been exploited for any application. Normally, silicon clusters are not thought of as being polar because of the four-times coordination of crystalline bulk silicon. However, a new allotropic form of silicon only appearing at nanoscale dimensions has recently been predicted theoretically, which leads to non-tetrahedral, ultrastable, and aromatic-like hydrogenated SiNCs with a strong permanent electric dipole moment.[15–23] Despite their apparently irregular structure some of those 1nm SiNCs can actually be more than 5 eV more stable than their well-known crystalline counterparts of the same size and stoichometry (see our Supporting Information for more details).[23,24]

In our present work, we use the inherent permanent dipole moment of those ultrastable nanoclusters to manipulate them with external electric fields. To this end, we keep the SiNCs trapped in a low-temperature plasma until they reach the target size and properties. One of the major advantages of using actually hydrogenated over pure SiNCs is the fact that their final structure and properties can largely be programmed by the flux ratio between atomic and molecular hydrogen in the plasma reactor.[18] A cluster target size of 1 nm has been chosen in our present work to assure that the clusters possess a strong permanent dipole moment.[23] We have analyzed their optical and electronic properties within an optical cavity using a supercontinuum light source and measured their permanent electric dipole moment *in situ* to be 2.2 ± 0.2 Debye. External electric fields were then used to spatially orient and guide these 1 nm building blocks for their controlled assembly on various substrates with the maximum deposition area roughly given by the physical size of the electrodes.[25] As a result, we present here the proof-of-concept that the simple presence of our ultrastable and well-aligned SiNCs on cathodes leads to a dramatic enhancement of the extracted electron current density which we predict will find immediate applications for a broad range of devices based on electron emission.

2 Experimental

2.1 Procedures to produce SiNCs with a permanent electric dipole moment

There are many different techniques to produce the presented non-tetrahedral SiNCs as, for example, deposition by chemical vapor processes, microwave plasmas, sputtering, micro-plasmas at atmospheric pressure, dielectric barrier discharges, pyrolysis or laser ablation. The only necessary condition for a successful SiNC generation is the ability to control both the nanocluster size and their silicon/hydrogen stoichiometry. Here, we have chosen to use a plasma enhanced chemical vapor deposition process (PECVD) because of its facility to generate a plethora of self-organized processes. As detailed below and in the Supporting Information, the PECVD method allows us to monitor very accurately the different phases of the cluster growth and thus to collect the desired nanoparticles with quasi-monodispersed size distributions for different applications. Of particular interest is the fact that a huge variety of precursor species (atoms, molecules, and radicals) are produced in a plasma combined with their different energetic characteristics (ranging from ionized, excited, metastable to ground state species). This mixture of species can lead to nanoscale assembling of entities with quite different atomic arrangements than what is expected from other production methods for nanoscale objects. The particular way of organisation leads, in turn, to significant differences in the physical, chemical, and optical properties of the produced nanomaterials.[26] Low-temperature silane plasmas are well-known media for the nucleation and growth of hydrogenated silicon nanoclusters (SiNCs).[27] Extensive experimental and theoretical studies have identified three growth phases of nanoparticles[28,29] (see Fig. S1 in Supporting Information). The most essential and critical one is the first phase, *i.e.*, a chemical phase that ends with the formation of 2-3 nm crystallites, depending on the experimental conditions used.[30,31] Due to the extremely small size of the produced particles, however, their con-

trolled deposition as building-blocks still presents a significant challenge. So far, only the modification of impact energy has been explored with charged nanoparticles.[32,33] The fact of producing neutral SiNCs with a permanent electric dipole moment allows us to orient them in space and guide them for self-assembly.

2.2 Generation of SiNCs in a PECVD plasma reactor

Inside a 0.02 m^3 vacuum chamber, an RF (13.56 MHz) CCP discharge was generated (Cesar 133 RF power supply) at low pressure between a grounded and a powered electrode. The circular electrode surfaces had a diameter of 7 cm and were separated by 4 cm. The shower-head shape of the powered electrode allowed the injection of a gas mixture of silane (2%) diluted in argon (98%) directly between the electrodes, in order to produce hydrogenated silicon nanoclusters in a pulsed discharge. The flow rate of the SiH_4/Ar gas mixture was controlled by a mass flow controller (MFC-Bronkhorst F-201DV, Low-ΔP-Flow), which was operated at a typical flow rate of 10 sccm.

As long as the plasma is switched on, the SiNCs are formed and trapped in the plasma bulk due to the negative charge they acquire by electron attachment. When the plasma is turned off, the SiNCs rapidly lose their negative charge to the positively charged argon ions by recombination. Then, they are swept down by the continuous gas flow. It has been shown that the velocity of the SiNCs between the electrodes is the same as the one of the gas flow.[34] As the gas flow is conserved when it enters the shower head electrode, the gas slows down because the diameter of the electrode $d(shower)$ is larger than the diameter of the tube $d(gas)$; *i.e.*, the gas flow velocity and, thus, the velocity of the nanoclusters $v(SiNC)$ between the electrodes is given by $v(SiNC) = v(gas, ini) \times [d(gas)/d(shower)]^2$ where $v(gas, ini)$ is the initial gas velocity in the tube. The resulting $v(SiNC)$ together with the distance of 4 cm between the electrodes gives us an estimate of roughly 200 ms for the time that the SiNCs need to travel between the two electrodes. Their mean free

path, using a hard spheres model, is of the order of 5.6 m that is very long compared to the distance between the two electrodes. This means that we can totally neglect collisions between individual SiNCs before their deposition.

A primary pump, which was connected to the chamber through an electronically controlled butterfly/throttle valve, was used to continuously remove the gas mixture from the chamber and maintain a constant low pressure of typically 0.12 mbar in the reactor. Under these conditions, the time required to fully remove residual gas from the vacuum chamber after a discharge pulse was estimated to be $\sim$1.5 s. This duration determined the typical time interval of 6 s between plasma discharge trigger pulses, which were generated by a specifically designed trigger board. A more detailed description of the trigger system is given below (also cf. Fig. 1b).

The gas was typically heated to 150 °C. At such a gas temperature, the formation of individual nanoparticles is ensured before they start agglomerating after about 6 seconds.[31] The discharge on-time was generally set to 2 s. Before experiments were performed, the chamber was fully pumped by a turbo pump overnight to a base pressure of $\sim 10^{-6}$ mbar while maintaining the chamber at 150 °C. The secondary pumping was done to clean the chamber and remove potential impurities.

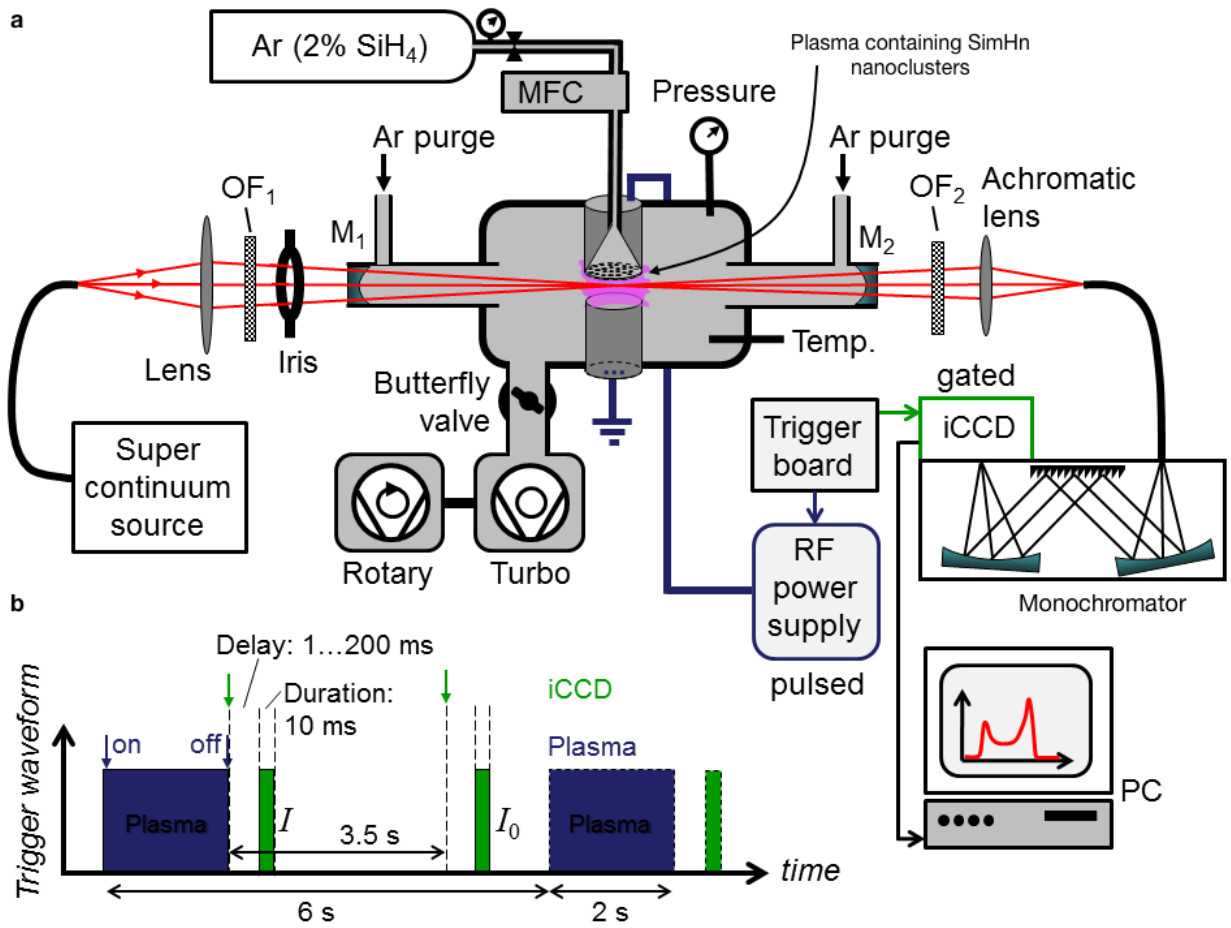

Figure 1: **Schematic of the experimental setup for the fabrication of SiNC-functionalized cathodes.** **a**, M_1 and M_2: high reflectivity (HR) mirrors ($R > 0.9997$). OF_1 and OF_2: combination of optical bandwidth and cut-off/on filters. The HR mirrors were purged with high-grade argon (99.999%); **b**, Typical trigger sequence to synchronise the gateable iCCD with the RF power supply. Blue: plasma triggers, green: iCCD triggers.

2.3 Incoherent broadband cavity-enhanced absorption spectroscopy (IBBCEAS) setup

IBBCEAS has been previously applied successfully in similar experiments to investigate the time-dependent extinction of naphthalene gas mixtures after multi-photon UV excitation.[35–37] In IBBCEAS, the extinction coefficient of a sample, $\varepsilon(\lambda)$, is determined by mea-

suring the transmission of light through an optically stable high-finesse cavity containing the sample species. The cavity is formed by two highly reflecting mirrors of reflectivity $R(\lambda)$. If the sample length, d, inside the cavity is known, then $\varepsilon(\lambda)$ [cm^{-1}] can be calculated:

$$\varepsilon(\lambda) = \frac{1 - R(\lambda)}{d}\left[\frac{I_0(\lambda)}{I(\lambda)} - 1\right] \tag{1}$$

where $I(\lambda)$ and $I_0(\lambda)$ are the wavelength-dependent intensities of light transmitted through the cavity with and without the target species in the sample zone, respectively; $R(\lambda)$ can be accurately determined by measuring the reflectivity as a function of wavelength using known concentrations of a calibration sample.[38]

The light source used in the absorption measurements was a spatially coherent supercontinuum light source (Fianium SC450) with a total output power of 5 W. It delivered pulses with a duration of ∼5 ps and was operated at a repetition rate of 50 MHz. Its emission covered a broad spectral range from ∼450 to 1800 nm; therefore appropriate combinations of long- and short-pass filters and/or bandpass filters were used to select a specific spectral region where the cavity mirrors are highly reflecting ($\Delta\lambda \approx \pm 30$ nm around the central wavelength). The light was coupled on-axis into the optical cavity for which the mirrors were connected to the reactor by vacuum flanges (see Fig. 1a). The cavity was formed by two plano-concave high-reflectivity (HR) mirrors (diameter 25 mm, radius of curvature -2 m) with a manufacturer-specified reflectivity of R > 0.9997. The separation of the cavity mirrors was 152 cm. This cavity length was chosen to maximise the distance between the discharge region and the mirrors in order to protect the mirrors from degradation due to their interaction with possibly reactive species formed in the plasma. Additionally, the mirrors were purged with a small argon flow at a rate of typically 10 sccm. Whenever the mirrors were not in use, they were isolated from the plasma reactor through large diameter gate valves. The wavelength-dependence of the reflectivity of the mirrors used in this experiment was determined independently using the method described elsewhere[39] and briefly explained

in the Supporting Information. Two different sets of mirrors were used, with HR regions centered at 610 nm (set 1) and 700 nm (set 2), respectively. The light transmitted exiting the cavity was focused with an achromatic lens (f = 3 cm) onto the 1 mm entrance aperture of a circular-to-rectangular multi-core fibre bundle. The fibre bundle was connected to the entrance slit of a polychromator (Shamrock 303i), which was used to disperse the light with a blazed diffraction grating of 600 lines/mm (corresponding to a spectral resolution of 0.65 nm). The light exiting the polychromator was detected with a gated iCCD (Andor iStar, DH740-18 mm). An optical filter after the cavity was used to protect the iCCD from exposure to excessive near infrared radiation.

Figs. S2, S3, and S4 in Supporting Information show a strong absorption peak in the visible region around 645 nm. The measured absorption spectra turn out to be in agreement with the absorption spectra of SiNCs with $Si_{19}H_{12}$ stoichiometry calculated at 0 K using the time-dependent density functional theory method.[20] At this point, we would like to note that, unlike the absorption measurements of single diatomic molecules, where the absorption bands often look very sharp and well-defined, we expect that the absorption band of a single nanocluster formed in a plasma reactor to be broader due to the thermal motion of a large number of cluster atoms under the experimental conditions. In addition, considering that our plasma conditions will not lead to the creation of one single isomer of $Si_{19}H_{12}$, but rather to a wide variety of similar SiNCs, we have to expect *a priori* that the effective total absorption extends over a relatively broad spectral region.

3 Results and Discussion

To confirm the theoretically predicted extraordinary electronic and optical properties of self-assembled, 1-nm-sized, plasma-born hydrogenated SiNCs, a capacitively coupled plasma (CCP) reactor for the production of those clusters was combined with a cavity enhanced absorption setup as a diagnostic tool. Due to the expectedly broad absorption features of

SiNCs in the visible wavelength region of interest and their potentially low concentration in the sample region of the reactor chamber, the technique of incoherent broadband cavity-enhanced absorption spectroscopy (IBBCEAS)[40] was used to detect extinction *in situ* in the plasma reactor. The components of the experimental setup are schematically shown in Fig. 1 and the detailed experimental conditions and procedures are described below in the Methods section. In the next section, the permanent electric dipole moment of the plasma-born SiNCs is evaluated. The formation of self-assembed ultra-thin silicon nanowires and the enhancement of thermionic current densities are then shown as two emerging applications.

3.1 Quantitative evaluation of the electric dipole moment

Previous theoretical studies have shown that self-assembled, non-tetrahedral, aromatic-like SiNCs of a size of 1 nm possess a strong permanent electric dipole moment.[23] In order to confirm and to explore such a characteristic quantitatively, we examined the effect of an applied DC electric field on the measured absorption spectra of those SiNCs. In Fig. 2, a schematic of the experimental setup and typical absorption measurements are shown for different DC bias voltages (for more details, see Methods). It is clear that the absorption decreases as the DC bias increases (red curves). One might be inclined to explain this decrease in the absorption signal as being due to charged particles moving under the influence of an electric field. However, a singly charged SiNC of this size placed in a 100 V DC bias takes only about 9 μs to cross the sample zone. The measurements, however, were taken 100 ms after the plasma was switched off and the DC bias switched on. Hence, even if the SiNCs were only singly charged, they would have crossed the light beam long before measurements were taken and, thus, no extinction would have been detected at all. Therefore, we can conclude that the majority of our SiNCs are electrically neutral and that the observed decrease in absorption is due to the fact that they possess a permanent electric dipole moment which is subjected to an inhomogeneous electric field between the two electrodes.

Simulations of the trajectories of the SiNCs starting from a region below the top electrode

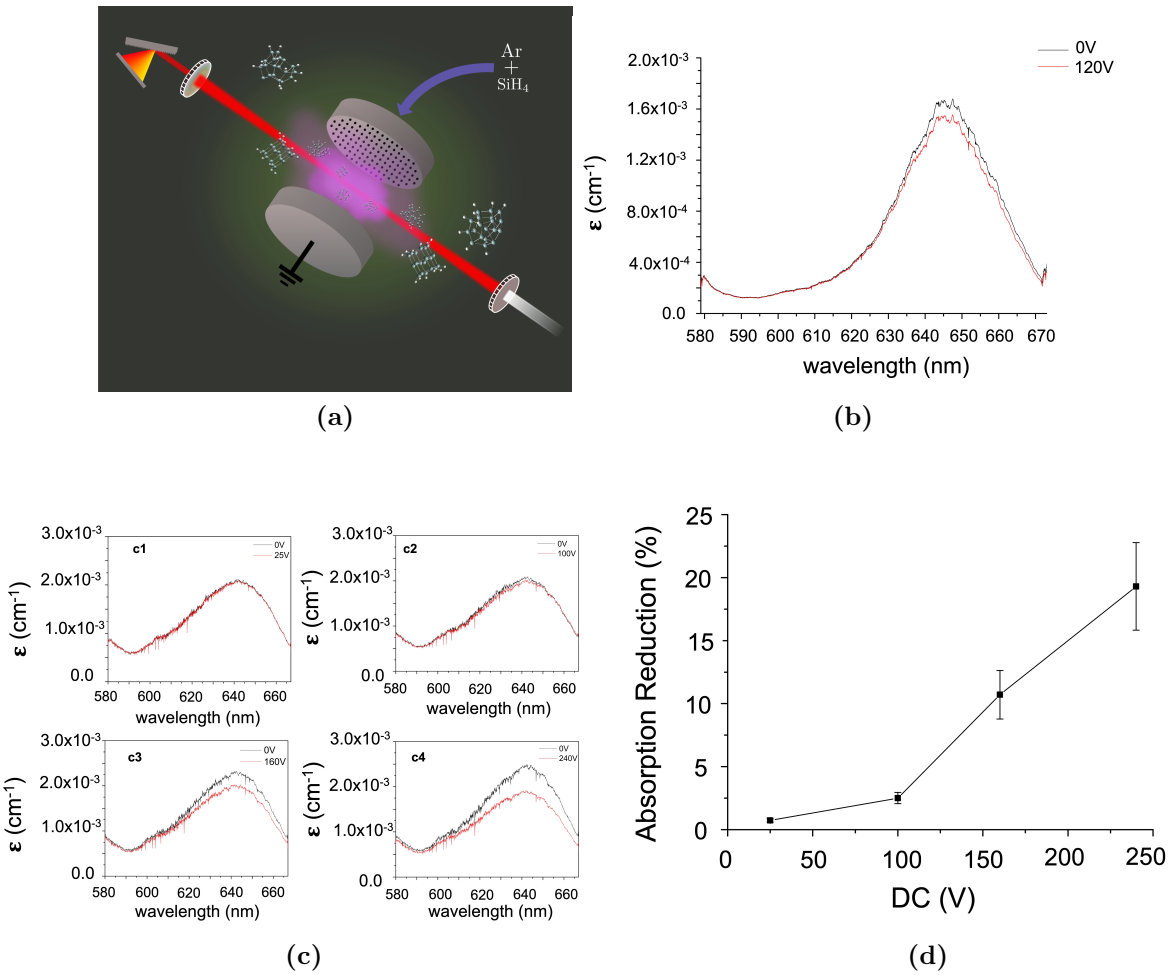

Figure 2: **Experimental proof that our SiNCs possess a permanent electric dipole moment.** **a**, Schematic of the experimental setup to measure optical absorption with and without an applied DC bias; **b**, Absorption spectra of SiNCs with an applied bias of 120 V compared to 0 V; **c**, a set of absorption measurements with and without an applied DC bias of 25 V in $\mathbf{c}_1$, 100 V in $\mathbf{c}_2$, 160 V in $\mathbf{c}_3$, and 240 V in $\mathbf{c}_4$; **d**, Plot of the reduction in the measured absorption in **c** as a function of the applied DC bias (see Methods for details). The error bars correspond to systematic errors and noise. The plasma duration is 2 s and the gate width and gate delay are 10 ms and 100 ms, respectively. The gas mixture flow is 10 sccm and the pressure and temperature of the gas are 0.115 mbar and 150 °C, respectively.

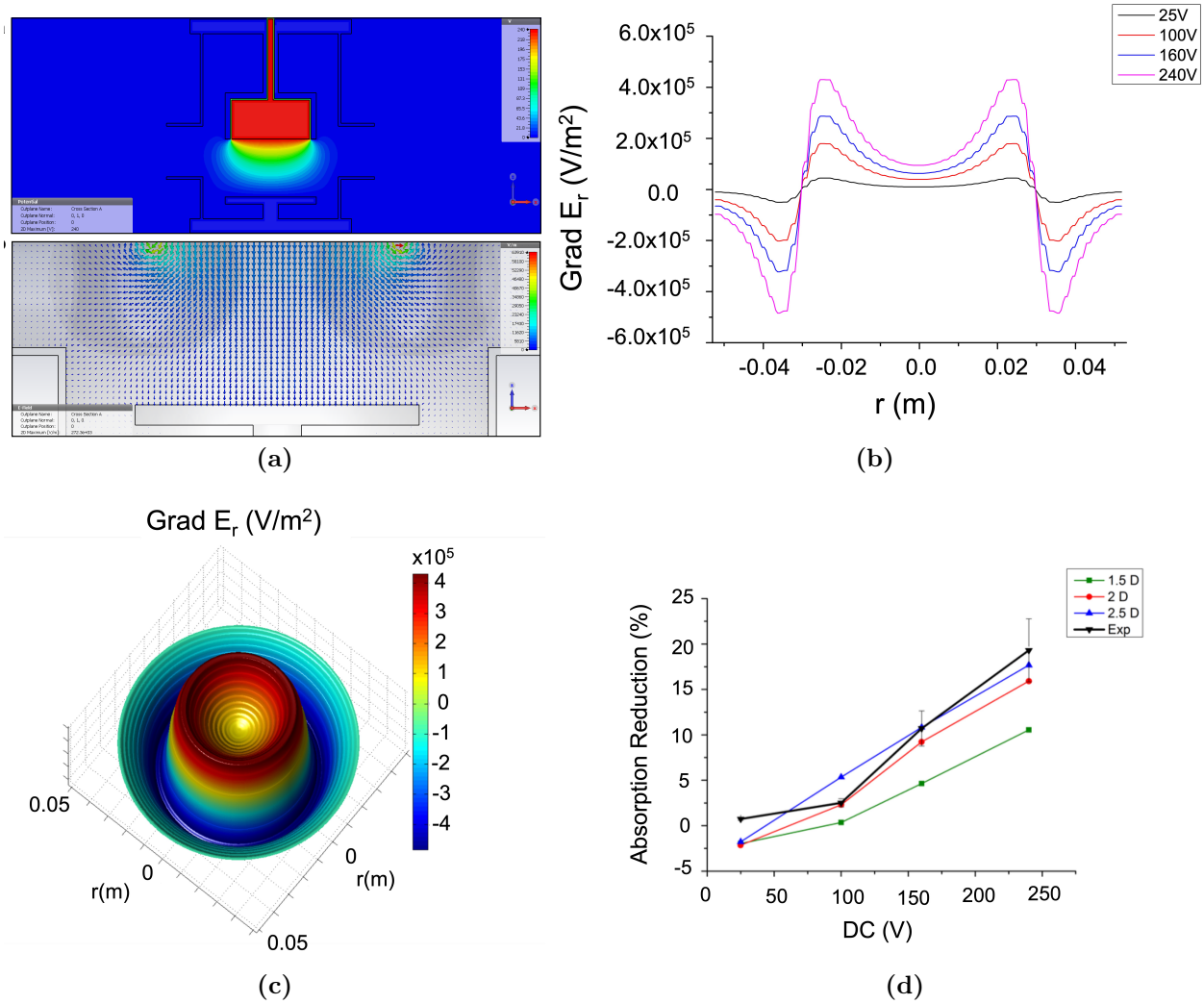

Figure 3: **Quantitative evaluation of the permanent electric dipole moment of our plasma-born SiNCs. a,** Upper panel: Simulated electric potential between the two electrodes - lower panel: Electric field vector map after applying a 240 V bias; **b,** The gradient of E_r along the radial direction for different applied bias voltages. For clarity, we show the gradient of E_r from the left side to the right side of the reactor; **c,** Three-dimensional representation of the gradient of E_r calculated for a 240 V bias; **d,** Plot of the reduction in the measured absorption and the calculated particle density as a function of the applied DC bias. The density of particles are obtained from trajectory simulations and are calculated for three values of the dipole moment of the SiNCs (1.5, 2.0 and 2.5 Debye).

until they reach the plane of the light beam were performed (see Methods). Fig. 3 shows the simulated percentage reduction in the average particle density as a function of the applied bias voltage for different assumed dipole moments in comparison to our measured reduction (values plotted in Fig. 2d). Clearly, the reduction in the density of particles possessing a dipole moment of 2.0 and 2.5 Debye agrees well with the reduction in the measured absorption and follows the same trend. Therefore, based on this combined theoretical and experimental analyses, we now have compelling evidence that our plasma-generated silicon nanoclusters with a size of about 1 nm possess a permanent dipole moment between 2.0 and 2.5 Debye. This result as well as the measured absorption spectra are in excellent agreement with previous estimations for individual $Si_{19}H_{12}$ isomers, based on *ab initio* calculations.[18,20,23] While this measured permanent dipole moment is, of course, significant smaller than the one known for nanorods of heavy metal compounds as, for instance, of cadmium selenide (CdSe),[41] we will show in the following that it is sufficiently strong for original and important applications.

3.2 Ultra-thin silicon nanowire formation

As a result of the measured permanent dipole moment, the direction of an applied DC electric field orients our plasma-born SiNCs in space, a possible spatial gradient of this electric field guides the SiNCs to specific substrate locations, and the dipole-dipole interaction between the aligned SiNCs assures the intra-cluster fine-adjustment for Silicon Nano Wire (SiNW) growth. We would like to mention that such a dipole-induced self-assembly growth for 1D SiNWs has recently been suggested for nanocubes with an electric dipole moment theoretically.[42] To confirm such a behavior experimentally, we recorded Atomic Force Microscopy (AFM) images of silicon wafer substrates after having been coated with our SiNCs for a deposition time of 1000 plasma pulses. We would like to remind that the reported SiNW growth was obtained without the use of any catalysts. The resulting images are shown in

Fig. 4. It is important to remember that the height resolution of a typical AFM is extremely high ($\sim$ 0.1 nm), while its lateral resolution is limited to approximately 10 to 20 nm.

As can be seen in Figs. 4d and 4f, the 1000 pulse deposition yields SiNWs with a length of up to 10 nm corresponding to the stacking of ten SiNCs for the vertical bias voltage. For the horizontal bias, however, only a maximum height modulation of about 1 nm can be observed (see Figs. 4c and 4e); *i.e.*, no SiNCs larger than 1 nm have been formed or deposited under our present experimental conditions. Analogously to the vertical bias, one can expect the formation of SiNWs lying in the surface plane for the horizontal bias. We have to remember, however, the considerable difference in lateral and height resolution of the AFM; *i.e.* if there is any SiNW growth of up to 10 nm in the horizontal direction, the AFM will not be able to resolve it. Nevertheless, we can conclude from the excellent height resolution of the AFM that the modulation amplitude of 1 nm gives a rough estimate for the maximum diameter of the grown SiNWs making them one of the thinnest SiNWs ever reported.[43]

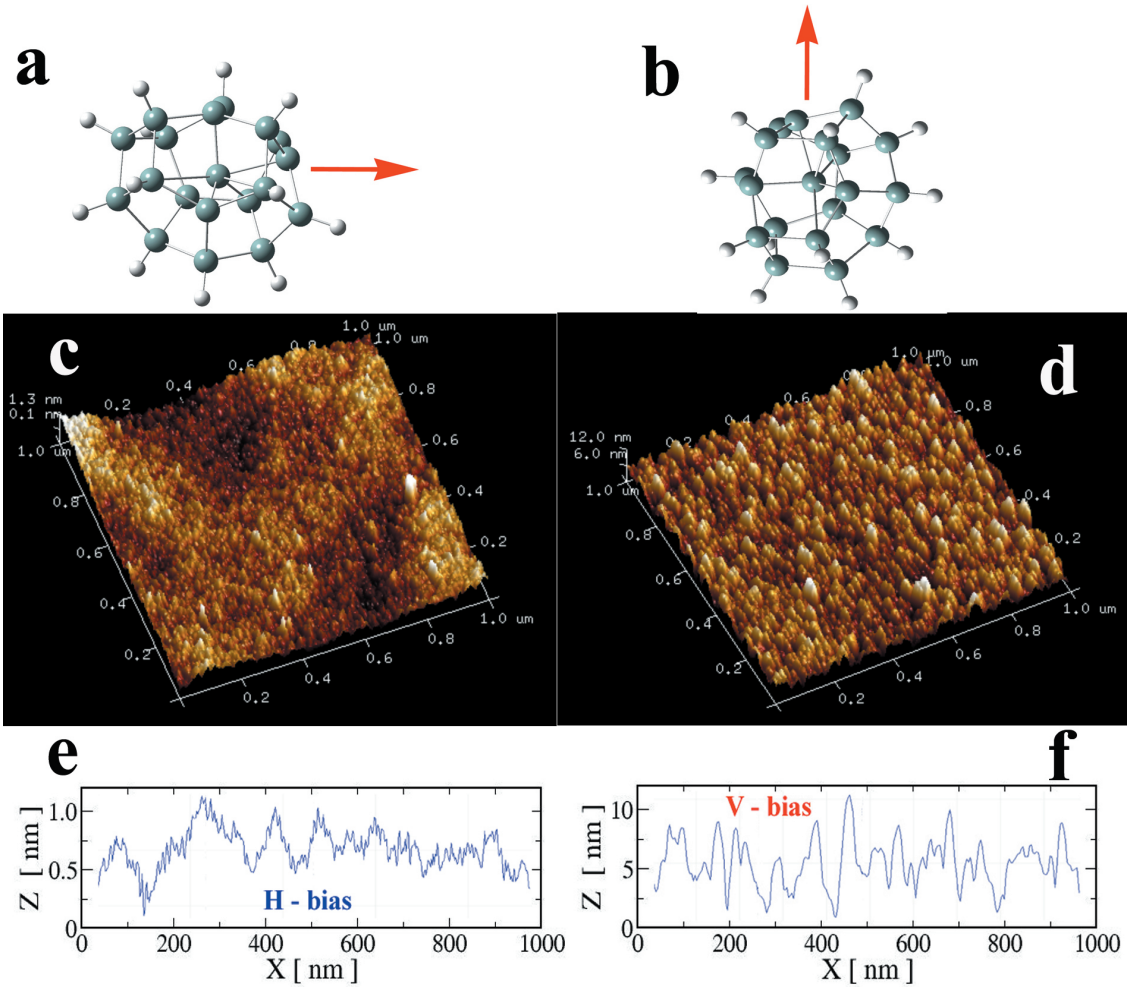

Figure 4: **AFM analysis of samples resulting from the surface deposition of dipole moment oriented SiNCs. a, b,** Ball and stick models of the most stable presently known 1 nm SiNCs[24] in two orthogonal dipole orientations; **c, d,** AFM images of two samples obtained with two orthogonal electric field orientations under otherwise identical plasma and deposition conditions; note the one order of magnitude difference in height; **e, f,** Corresponding measured height profiles giving quantitative information on the height and diameter of the ultra-thin silicon nanowires formed by self-assembly without any catalyst from the 1 nm building blocks shown in **a** and **b**.

3.3 Proof-of-concept: thermionic current density enhancement

Devices that depend on the efficient emission of electrons are omnipresent in our daily lives as for examples, cathode ray tubes, mass spectrometers, electron microscopes, welding machines, metal coating machines, 3D metal printers, vacuum furnaces, production of X-rays,

and electric thrusters used in spacecrafts and satellites. The efficiency of the involved electron guns depends on the work function (WF) of the employed cathode material; *i.e.* on the minimum energy for electron extraction. In recent years, LaB_6 has become a material of choice in many areas where efficient electron extraction plays a crucial role because of its low work function that can be as small as 2.7 eV after proper preparation.[44] While being much easier to handle than cesium, which is known to be the element with the lowest WF (2.1 eV), LaB_6 still requires annealing to above 1000°C prior to usage, it progressively evaporates during operation, and has a WF that is still considerably higher than the one of cesium.

Methods to reduce the WF have previously been proposed. One rather efficient method regrettably involves the incorporation of extremely toxic, volatile, and expensive transition metals.[45] Very recently, light-induced WF modulations have been reported;[46] unluckily, it only concerns expensive noble metals that intrinsically possess some of the highest known WF in their elemental form. It is well known that the presence of molecular entities with a permanent dipole moment, as for instance, organic self-assembled monolayers (SAMs), can modify the WF of their substrate material; *i.e.*, the energy necessary for the extraction of electrons can either be increased or decreased dependent on the spatial orientation of the dipole moments.[47–49] The SAMs proposed up-to-date, however, cannot withstand high temperatures as necessary, for instance, in propulsion engines.

One can easily imagine to replace those organic SAMs by ultrastable SiNCs with a permanent electric dipole moment. Based on the observed continuous growth of SiNWs for increased deposition times, we can actually conclude that the permanent electric dipole moment of our SiNCs even survives after their surface deposition. Therefore, we will explore the possibility to modify the thermionic electron current density of a given material with our SiNCs. The present experimental setup is perfectly adopted for this study because, as shown above, our SiNCs are readily orientated in space by the direction of an applied DC electric field due to their dipole moment before their surface deposition.

In the following, we will thus explore the efficiency of electron extraction based on

thermionic emission for sintered lanthanum hexaboride (LaB_6) cathodes. To this end, the thermionic current densities are comparatively measured for a pristine LaB_6 cathode and for one coated with our SiNWs as above. Fig. 5a gives a simplified diagram of the experimental setup. The measurements take place in a vacuum chamber at a working pressure of 3×10^{-5} mbar. A relatively low base pressure is needed to limit secondary plasma formation and to avoid arcing. The cathode pellets are encapsulated in an insulator placed on top of a grounded planar heater. The heating circuit is electrically insulated from the rest of the setup not to disturb the cathode potential and the current flow. The cathode material temperature is measured using a type C thermocouple that can be operated up to 1200 °C. A ceramic spacer with a hole of 8 mm diameter is placed in between the cathode and the anode. The hole is aligned with the cathode axis for the electron current to flow. The cathode-anode gap is 2.8 mm. An electric field is generated by the application of a positive voltage, up to 1 kV, on the anode. The thermionic electron current collected on the anode is measured using a calibrated Keithley 2410 picoampermeter. Fig. 5b demonstrates that the measured current density of the extracted electrons can be enhanced by a factor as high as 30 due to the simple presence of our SiNCs. According to the Richardson-Dushman law[50,51] as expressed in equation (1) in Supporting Information, the two curves approach each other for very high temperatures. Due to the Schottky effect the extracted electron current density can be enhanced by a factor of nearly 5 at an applied voltage of 1000 V (see Fig. 5c). In Fig. 5d, we plotted the logarithm of the current density as function of the square root of the voltage to confirm the linear dependence in the Schottky regime as predicted by equation (5) in Supporting Information. Extrapolation of those straight lines to zero voltage permits us to estimate a difference in work function of roughly 0.46 eV between the uncoated and the coated LaB_6 cathodes. As can, for instance, be seen in Fig. 5b, such a difference in WF causes the current density coming from the uncoated LaB_6 cathode at 500 °C to be about the same as the one at only 250 °C for the coated material. The corresponding devices can, thus, be operated at significantly lower temperatures increasing their lifetime and reducing

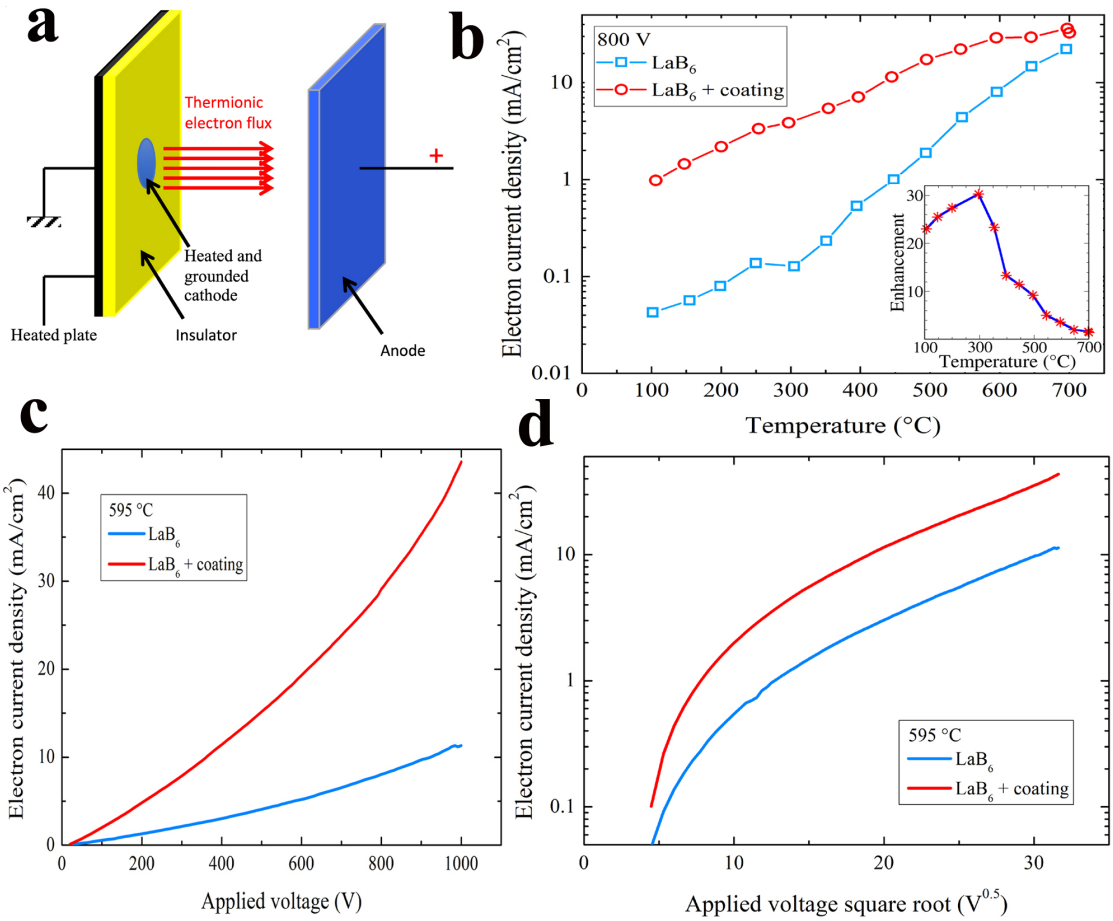

Figure 5: **Enhancement of thermionic current densities.** **a,** Schematic of the experimental setup for the measurement of the current density of the extracted electrons; **b,** Evolution of the electron current density with temperature for a pristine LaB_6 cathode (blue) and a SiNCs coated LaB_6 cathode (red); the relative enhancement factor of the current density is shown in the inset demonstrating the intensification of the thermionic effect; **c,** Electron current density against cathode-anode voltage for coated (red) and uncoated (blue) LaB_6 emitters demonstrating the enhancement of the Schottky effect; **d,** Evolution of the logarithm of the electron current density with the square root of the voltage; the linear part corresponds to the Schottky regime (see Methods for details).

energy consumption as well as cathode material evaporation. In addition, we claim that the SiNC coating plays an important role in yet further preventing the loss of cathode material at a given temperature and in protecting the substrate material against environment-induced degradation. The maximum area treated by our SiNCs is roughly given by the size of the reactor electrodes, which can largely exceed $1m^2$ for industrial PECVD reactors.[25]

Considering the presence of SiNWs on our LaB_6 cathodes, we cannot *a priori* exclude the possible action of electron field emission. However, comparing the relative enhancement with applied temperature and electric field as shown in Figs. 5b and 5c, respectively, we can certainly conclude that the role of thermionic emission is largely dominant under our present experimental conditions. This conclusion is also supported by the linear behavior in the Schottky regime when the logarithm of the current density is expressed as a function of the square root of the applied voltage; see Fig. 5d and equation (5) in Supporting Information.[52]

Finally, we would like to address the question of durability of our proposed SiNC coatings briefly. At present, the most promising applications for our SiNCs seem to be for the negative ion generation in thermonuclear fusion reactors and for cathodes in satellite thrusters. In both examples, high resistance against ion sputtering is crucial and it turns out that silicon is one of the elements with the lowest ion sputtering yield in the huge range from low-energy (subthreshold) sputtering until at least 100keV.[53–56] Only titanium, beryllium, and carbon have similar or slightly lower sputtering yields indicating that whatever the cathode material might be, our SiNC coating will improve its resistance toward ion sputtering.

4 Conclusions

We have shown that hydrogenated SiNCs with a permanent electric dipole moment can readily be produced and spectroscopically studied in a plasma reactor. This dipole moment has permitted us to manipulate individual SiNCs for the nanoarchitecture of one of the

thinnest nanowires yet observed. Motivated by the need of high performance cathodes for many daily applications, we have then used those SiNCs with a strong permanent electric dipole moment to reduce the work function of LaB_6 cathodes. We have shown that the simple presence of our SiNCs readily leads to an increase of the measured electron current density by a factor of 30 even for LaB_6 cathodes that have already become a reference material for all devices for which efficient electron ejection is crucial. For the incorporation of SiNC-functionalized cathodes in electron gun devices, we thus predict either a considerable increase in current density for a given operational temperature or a significant reduction in operation temperature for a given target current density. In addition, the possible evaporation of cathode material becomes nearly impossible due to the extreme stability of the deposited SiNC layer.

We have provided the first proof-of-concept of a simple, but powerful method to modify the WF of materials that will find many far-reaching immediate applications; we only like to mention here optimized electron injection and extraction for flexible electronics,[57] improved performance for lithium ion batteries,[58] enhanced emission for all electron gun devices as electron microscopes, mass spectrometers, accelerators *etc.*, high-performance electrodes even for biomedical applications *e.g.* invasive and non-invasive brain-computer interfaces,[59,60] and cesium-free negative ion production for more environment-friendly nuclear fusion reactors. The quantitative measurement of an absolute WF requires many precautions and calibrations. Therefore, we plan a more in-depth study in the future to evaluate the resulting WFs quantitatively with precision; here, we just want to demonstrate the possibility to enhance the thermionic current density significantly due to the permanent electric dipole moment of our SiNCs. Future work is planned to understand better the interplay of all experimental parameters to obtain the lowest possible WF. To this end, the ideal SiNW length, the best plasma temperature, and the optimal hydrogen contents *etc.* remain to be determined.

5 METHODS

5.1 Effect of a DC electric field on plasma-born SiNCs

If the electric field is homogeneous, it will only provide a torque that orients the molecular dipole moment, $\vec{p}$, along the electric field lines. However, if it is an inhomogeneous electric field, it will not only orient, but also exert a force on the polar cluster to displace it since the forces on the positive and negative charges of the dipole do not cancel each other exactly. Hence, the field provides an overall force on the cluster given by $\vec{F} = \nabla(\vec{p} \cdot \vec{E})$. Fig. 2b shows the absorption measured with an applied DC bias of 120 V compared to the absorption measured without any bias. The absorption decreases in the presence of a DC bias (red curve). As discussed above, the SiNCs are neutral. The observed change in absorption in the presence of an inhomogeneous electric field, can thus be understood by the fact that our SiNCs do possess a permanent electric dipole moment; *i.e.* the dipole forces acting on the SiNCs affect their translation during their drift due to the gas flow, resulting in a change in their density distribution and, hence, in the absorption signal.

To explore how the absorption changes as function of the applied DC bias, we have performed a set of absorption measurements with and without an applied electric field for a range of DC bias voltages (25, 100, 160 and 240 V) under the same experimental conditions as before. Fig. 2c shows the measured absorption with an applied bias compared to that without any bias. In all measurements, we find a decrease in the absorption signal in the presence of an applied electric field. This decrease depends on the strength of the applied field. In order to clarify this dependence, the percentage of the reduction in the absorption ($\frac{\epsilon_{0V} - \epsilon_{DC}}{\epsilon_{0V}} \times 100$) as a function of the DC bias is shown in Fig. 2d. Between 25 and 100 V there is only a slight decrease in absorption. However, the decrease in the absorption starts to increase approximately linearly with higher DC bias voltages.

In order to provide a quantitative estimation of the permanent dipole moment of those

plasma-born, non-tetrahedral, 1 nm sized SiNCs, a better understanding of the inhomogeneity of the electric field in the reactor chamber is important; *i.e.* the inhomogeneity of the electric field as a function of the radius measured from the center of the electrode (*Grad* E_r) influences the movement of the nanoclusters and, hence, their distribution in the plane of the light beam. To this end, simulations of the electric field employing the finite elements method using a 3D electrostatic solver were performed.[61] Fig. S5 in Supporting Information shows a cross-sectional view of the reactor chamber with its exact configuration and dimensions. In Fig. 3a, we show the potential (upper panel) and the electric field vector map (lower panel) for a 240 V DC bias. It is clear from the vector map that the electric field is symmetric in the reactor; it is mostly homogeneous in the center (vertical arrows), and strongly inhomogeneous near the edges of the top electrode.

In Fig. 3b, we plot the gradient of E_r along the radial direction for a range of potentials (25 V, 100 V, 160 V and 240 V), which is similar for all rays with any angle θ in the polar system due to cylindrical symmetry (see Fig. 3c for a 3D representation calculated for the 240 V bias). Fig. 3b illustrates that the gradients of E_r, which represent the dipole forces, are positive in the center of the reactor and progressively increase until about 24 mm from the center. After that, the forces show a sudden drop and become negative around 30 mm. Then, they start to increase again keeping a negative sign up to approximately 36 mm (*i.e.* this distance corresponds to about the radius of the electrode). Finally, the forces decrease again but remain negative until the walls of the reactor. This means that the dipole forces act on the nanoclusters in such a way that they push them toward the reactor walls as long as they are positive and toward the center of the reactor when they are negative. Generally speaking, while the SiNCs are moving toward the detection beam in the presence of an applied inhomogeneous electric field, they spread out under the influence of the dipole forces. Thus, a new distribution of SiNCs is established within a plane, located parallel to the electrode. The density distribution of SiNCs in that plane is a function of the applied bias voltage and gradually changes as the plane approaches the detection beam.

5.2 Experimental synchronisation between plasma pulses and absorption measurements

A trigger board synchronised the plasma discharge with the gated detector. As shown schematically in Fig. 1b, the trigger board generated three trigger pulses. The *initial* trigger pulse determined the start and the duration of the plasma discharge (indicated by blue arrows in Fig. 1b). The falling edge of the initial pulse triggered two subsequent trigger pulses for the iCCD (indicated by green arrows). The *first* of these two pulses is generated immediately on the falling edge of the "plasma pulse" and was used to record the cavity transmission with the sample ($I(\lambda)$ in equation (1)) shortly after the end of the discharge plasma, the *second* pulse was always generated 3.5 s later and triggered the measurement of the cavity transmission without the sample ($I_0(\lambda)$ in equation (1)), *i.e.* without SiNCs. The two pulses for the detector triggered a digital delay and a gate generator of the iCCD. The delay time and gate width (= integration time) could freely be chosen (vertical dashed lines in Fig. 1b), but are the same for the measurements of I and I_0. The gate width was 10 ms in all cases. The gate delay, however, was varied for different experiments between $\sim$ 1 and $\sim$ 200 ms. The time difference of 3.5 s between the two pulses for the iCCD (green puless) was sufficiently long to ensure that any residual nanoclusters were pumped out of the reactor between recording the sample (I) and the background (I_0) transmission. Typical spectra were averaged over 100 to 1000 plasma pulses.

We stress here that our technique in measuring I and I_0 alternatingly between plasma pulses, rather than subsequently at the end of the total number of pulses, has the advantage that systematic errors, such as light source fluctuations, variations in residual optical losses due to scattering, very gradual misalignment effects or mirror drifts, and slow and small pressure variations, are effectively reduced due to the short time separation between the respective measurements of I and I_0.

5.3 Experimental synchronisation between SiNC production and the applied DC bias voltage during their deposition

A DC bias was applied between the top and bottom electrodes when the plasma was turned off. To this end, one more trigger pulse was added to the trigger board to determine the start and stop of the applied DC bias. In order to eliminate any issues from drifting cavity alignment, these two measurements were carried out concurrently, *i.e.* the measurements alternated, shot-by-shot, between measuring the extinction with an applied bias, and measuring it without a bias. The plasma duration was 2 s. The measurements were taken with a 10 ms gate after a 100 ms delay. The gas pressure and temperature were 0.115 mbar and 150 °C, respectively, with a gas mixture (SiH_4/Ar) flow rate of 10 sccm.

5.4 Particle trajectory simulations necessary for dipole evaluation

At the instant the plasma is switched off, the SiNCs are mainly equally distributed in a region under the powered electrode. Thus, in the absence of any applied DC bias, the SiNCs approximately reach the detection beam plane keeping their initial distribution.[62] However, in the presence of a DC bias, the SiNCs attain a new distribution. In order to gain a deeper insight into the density of the SiNCs in the detection beam plane within the flow, we simulated their trajectories from their initial positions in a region below the top electrode until they reach the light beam, where we obtain their new distribution. The simulations were performed as follows:

- We start with an equal density distribution of particles in each 1 mm ring section in a plane that is 5 mm below the top electrode (see Fig. S7 in Supporting Information for an illustration). The mass of the particle corresponds to the mass of a $Si_{19}H_{12}$ nanocluster (*i.e.* 546 amu).

- Using Newton's equations of motion, we follow the trajectory of the particles under the influence of the dipole forces (calculated from the gradient of E_r) with a time step of 1 ms until they reach the plane of the detection beam. Thus, we obtain the final position of each particle in that plane.

- From the number of particles in each ring section, we find the new densities and, hence, the new distribution of particles.

To determine the percentage in the change of the average density of the SiNCs to which our light extension measurement is sensitive, calculated in the plane of the detection beam, in the presence and absence of a DC bias, we follow the same procedure as above for the absorption measurements (see Fig. 2d). A comparison between these two situations has mainly shown a reduction in the average density of the SiNCs in the presence of a DC bias; this reduction depends on the applied DC field. We have performed the above analysis for particles possessing a dipole moment of 1.5, 2.0 and 2.5 Debye, respectively. Fig. 3d shows the percentage reduction in the average density of particles as a function of the applied bias for the different dipole moments, compared to the reduction in the absorption obtained from our experiments (values plotted in Fig. 2d). We notice that only for 25 V, we obtain from our simulations a slight increase in the density of particles ($\sim$2%) in the presence of the applied bias (instead of a slight decrease) for the three selected dipole moment cases. This is due to the confinement of some particles in a region that is immediately below the top electrode. However, for all other DC biases, we find a reduction in the calculated density that depends on the applied bias, *i.e.* on the strength of the dipole forces acting on the particles, and thus on the way and the number of particles that participate in the redistribution in the different rings in the plane of the detection beam (see trajectories simulations in Supporting Information). The resulting simulated reduction in the density of particles possessing a dipole moment of 2.0 Debye and 2.5 Debye, agrees well with the reduction in the measured absorption and follows the same trend.

Supporting Information

The life stages of dust particles; a short history of non-tetrahedral, ultrastable, and aromatic-like silicon nano clusters (SiNCs); measured *in-situ* absorption spectra of plasma-born SiNCs; a schematic representation of the reactor chamber; dipole forces acting on SiNCs along the z-axis; deconvolution of particle density distributions from trajectories simulations; a short movie illustrating the silicon nanowire growth; basics of thermionic electron emission; and mirror reflectivity calibration for incoherent broadband cavity-enhanced absorption spectroscopy. This material is available free of charge via the Internet at http://pubs.acs.org.

Acknowledgments

Funding: This work was made possible through the financial support of the CNRS. In particular, we gratefully acknowledge the efficient help of CNRS in the framework of their Innovation prematuration 2020 program. The HPC centers of IDRIS (Grant A0060900642) and CERMM are acknowledged for computational resources and the Hariri Foundation for Sustainable Human Development for the scholarship awarded to F. J. This publication has emanated from research conducted with the financial support of Science Foundation Ireland under Grant number [11/RFP.1/PHY/3233]. **Support:** The present work would not have been possible without the precious help of Professor David Graves at UC Berkeley in the early phases of this project. We like to express our gratitude to Professor André Bouchoule for his careful reading of the manuscript. **Competing Interests:** The authors declare that they have no competing interests. **Data and materials availability:** All data needed to evaluate the conclusions in the paper are present in the paper and/or the Supporting Information. Additional data related to this paper may be requested from the authors.

References

(1) Hollenstein, C. The physics and chemistry of dusty plasmas. *Plasma Phys. Control. Fusion* **2000**, *42*, R93–R104.

(2) Chen, X.; Seto, T.; Kortshagen, U. R.; Hogan, C. J. Size and structural characterization of Si nanocrystal aggregates from a low pressure nonthermal plasma reactor. *Powder Technology* **2020**, *373*.

(3) Curtis, I. S.; Wills, R. J.; Dasog, M. Photocatalytic hydrogen generation using mesoporous silicon nanoparticles: influence of magnesiothermic reduction conditions and nanoparticle aging on the catalytic activity. *Nanoscale* **2021**, *13*, 2685–2692.

(4) Mussabek, G.; Alekseev, S. A.; Manilov, A. I.; Tutashkonko, S.; Nychyporuk, T.; Shabdan, Y.; Amirkhanova, G.; Litvinenko, S. V.; Skryshevsky, V. A.; Lysenko, V. Kinetics of Hydrogen Generation from Oxidation of Hydrogenated Silicon Nanocrystals in Aqueous Solutions. *Nanomaterials* **2020**, *10*, 1413.

(5) Abdalla, Y.; Luo, M.; Mäkilä, E.; Day, B. W.; Voelcker, N. H.; Tong, W. Y. Effectiveness of porous silicon nanoparticle treatment at inhibiting the migration of a heterogeneous glioma cell population. *J Nanobiotechnology* **2021**, *19*, 1–16.

(6) Tokarska, K.; Shi, Q.; Otulakowski, L.; Wrobel, P.; Ta, H. Q.; Kurtyka, P.; Kordyka, A.; Siwy, M.; Vasylieva, M.; Forys, A.; Trzebicka, B.; Bachmatiuk, A.; Rümmeli, M. H. Facile production of ultra-fine silicon nanoparticles. *Royal Society Open Science* **2020**, *7*, 200736.

(7) Abe, T.; Iwamoto, T.; Kira, M. A stable 1,2-disilacyclohexene and its 14-electron palladium(0) complex. *J. Am. Chem. Soc.* **2010**, *132*, 5008–5009.

(8) Keuter, J.; Schwermann, C.; Hepp, A.; Bergander, K.; Droste, J.; Hansen, M. R.;

Doltsinis, N. L.; Mück-Lichtenfeld, C.; Lips, F. A highly unsaturated six-vertex amido-substituted silicon cluster. *Chem. Sci.* **2020**, *23*, 5895–5901.

(9) Abersfelder, K.; White, A. J. P.; Berger, R. J. F.; Rzepa, D., H. S.and Scheschkewitz A Stable Derivative of the Global Minimum on the Si(6)H(6) Potential Energy Surface". *Angew. Chem., Int. Ed.* **2011**, *50*, 7936–7939.

(10) Bedini, A. P. C. Sonochemical synthesis of hydrogenated amorphous silicon nanoparticles from liquid trisilane at ambient temperature and pressure. *Ultrasonics - Sonochemistry* **2017**, *39*, 883–888.

(11) Accolla, M.; Santoro, G.; Merino, P.; Martínez, L.; Tajuelo-Castilla, G.; Vázquez, L.; Sobrado, J. M.; Agúndez, M.; Jiménez-Redondo, M.; Herrero, V. J.; Tanarro, I.; Cernicharo, J.; Martín-Gago, J. Á. Silicon and Hydrogen Chemistry under Laboratory Conditions Mimicking the Atmosphere of Evolved Stars. *The Astrophysical Journal* **2021**, *906*, 44.

(12) Wang, M. Suppressing material loss in the visible and near-infrared range for functional nanophotonics using bandgap engineering. *Nature Communications* **2020**,

(13) Wang, X.; Zhang, R. Q.; Lee, S. T.; Niehaus, T. A.; Frauenheim, T. Unusual size dependence of the optical emission gap in small hydrogenated silicon nanoparticles. *Applied Physics Letters* **2007**, *90*, 123116.

(14) Le, H.-L. T.; Jardali, F.; Vach, H. Deposition of hydrogenated silicon clusters for efficient epitaxial growth. *Physical Chemistry Chemical Physics* **2018**, *20*, 15626–15634.

(15) Hanlon, P. From nanocrystals to DVD. *Nature Materials* **2005**, *4*, 878.

(16) Chun, A. L.; Rodgers, P.; Segal, M.; Vaughan, O. Silicon nanocrystals: More is better. *Nature Nanotech* **2011**, *5*, 756.

(17) Rodgers, P. Briefings in Nanotechnology. *Scientific American* **2012**, *1*, 5.

(18) Vach, H.; Brulin, Q. Controlled growth of silicon nanocrystals in a plasma reactor. *Phys. Rev. Lett.* **2005**, *95*, 165502.

(19) Vach, H. Ultrastable silicon nanocrystals due to electron delocalization. *Nano Lett.* **2011**, *11*, 5477–5481.

(20) Vach, H.; Ivanova, L. V.; Timerghazin, Q. K.; Jardali, F.; Le, H. L. T. Metallic-like bonding in plasma-born silicon nanocrystals for nanoscale bandgap engineering. *Nanoscale* **2016**, *8*, 18062–18069.

(21) Vach, H. Electron-deficiency aromaticity in silicon nanoclusters. *J. Chem. Theory Comput.* **2012**, *8*, 2088–2094.

(22) Vach, H. Terahertz and Gigahertz emission from an all-silicon nanocrystal. *Phys. Rev. Lett.* **2014**, *112*, 197401.

(23) Vach, H. Symmetric and irregular aromatic silicon nanoclusters. *Chem. Phys. Lett.* **2014**, *614*, 199–203.

(24) Gordeychuk, M. V.; Katin, K. P.; Grishakov, K. S.; Maslov, M. M. Silicon buckyballs versus prismanes: Influence of spatial confinement on the structural properties and optical spectra of the $Si_{18}H_{12}$ and $Si_{19}H_{12}$ clusters. *Int. J. Quantum Chem.* **2018**, *118*, e25609.

(25) Sansonnens, L.; Schmidt, J.; Howling, A. A.; Hollenstein, C.; Ellert, C.; Buechel, A. Application of the shaped electrode technique to a large area rectangular capacitively coupled plasma reactor to suppress standing wave nonuniformity. *Journal of Vacuum Science & Technology A* **2006**, *24*, 1425–1430.

(26) Ostrikov, K.; Neyts, E. C.; Meyyappan, M. Plasma Nanoscience: From nano-solids in plasmas to nano-plasmas in solids. *Adv. Phys.* **2013**, *62*, 113–224.

(27) Bouchoule, A. *Dusty plasma: Physics, chemistry and technological impacts in plasma processing*; New York: Wiley: New York, 1999.

(28) Boufendi, L.; Bouchoule, A. Particle nucleation and growth in a low-temperature argon-silane discharge. *Plasma Sources Sci. Technol.* **1994**, *3*, 262–267.

(29) Fridman, A. A.; Boufendi, L.; Hbid, T.; Potapkin, B. V.; Bouchoule, A. Dusty plasma formation: Physics and critical phenomena. Theoretical approach. *J. Appl. Phys.* **1996**, *79*, 1303–1313.

(30) Viera, G.; Huet, S.; Boufendi, L. Crystal size and temperature measurements in nanostructured silicon using Raman spectroscopy. *J. Appl. Phys.* **2001**, *90*, 4175–4183.

(31) Boufendi, L.; Jouanny, M.; Berndt, E. K. J.; Mikikian, M. Dusty plasma for nanotechnology. *J. Phys. D: Appl. Phys.,* **2011**, *44*, 174035.

(32) Larriba-Andaluz, C.; Girshick, S. L. Controlled Fluxes of Silicon Nanoparticles to a Substrate in Pulsed Radio-Frequency Argon–Silane Plasmas. *Plas. Chem. Plas. Process.* **2017**, *37*, 43–58.

(33) Chaâbane, N.; Suendo, V.; Vach, H.; Cabarrocas, P. R. Soft landing of silicon nanocrystals in plasma enhanced chemical vapor deposition. *Appl. Phys. Lett.* **2006**, *88*, 203111 – 203111.

(34) Boufendi, L.; Bouchoule, A.; Porteous, R. K.; Blondeau, J. P.; Plain, A.; Laure, C. Particle–particle interactions in dusty plasmas. *Journal of Applied Physics* **1993**, *73*, 2160–2162.

(35) Ruth, A. A.; Gash, E. W.; Staak, M.; Fiedler, S. E. Multi-photon UV photolysis of naphthalene-gas mixtures: A new gas-phase oscillatory system. *Phys. Chem. Chem. Phys.* **2002**, *4*, 5217–5220.

(36) Walsh, A. J.; Ruth, A. A.; Gash, E. W.; Mansfield, M. W. D. Multi-photon UV photolysis of gaseous polycyclic aromatic hydrocarbons: Extinction spectra and dynamics. *J. Chem. Phys.* **2013**, *139*, 054304.

(37) Walsh, A. J.; Tielens, A. G. G. M.; Ruth, A. A. Diamond-like-carbon nanoparticle production and agglomeration following UV multi-photon excitation of static naphtalene/helium gas mixtures. *J. Chem. Phys.* **2016**, *145*, 024303.

(38) Venables, D. S.; Gherman, T.; Orphal, J.; Wenger, J. C.; Ruth, A. A. High Sensitivity in Situ Monitoring of NO_3 in an Atmospheric Simulation Chamber Using Incoherent Broadband Cavity-Enhanced Absorption Spectroscopy. *Environ. Sci. Technol.* **2006**, *40*, 6758–6763.

(39) Washenfelder, R. A.; Langford, A. O.; Fuchs, H.; Brown, S. S. Measurement of glyoxal using an incoherent broadband cavity enhanced absorption spectroscometer. *Atmos. Chem. Phys.* **2008**, *8*, 7779–7793.

(40) Fiedler, S. E.; Hese, A.; Ruth, A. A. Incoherent broad-band cavity-enhanced absorption spectroscopy. *Chem. Phys. Lett.* **2003**, *371*, 284–294.

(41) Li, L.-S.; Alivisatos, A. P. Origin and scaling of the permanent dipole moment in CdSe nanorods. *Phys Rev Lett* **2003**, *90*, 097402.

(42) Zhang, X.; Zhang, Z.; Glotzer, S. C. Simulation Study of Dipole-Induced Self-Assembly of Nanocubes. *The Journal of Physical Chemistry C* **2007**, *111*, 4132–4137.

(43) Tan, Z.; Shi, W.; Guo, C.; Zhang, Q.; Yang, L.; Wu, X.; Cheng, G.-a.; Zheng, R. Fabrication of ultra-thin silicon nanowire arrays using ion beam assisted chemical etching. *Nanoscale* **2015**, *7*, 17268–17273.

(44) Pelletier, J.; Pomot, C. Work function of sintered lanthanum hexaboride. *Appl. Phys. Lett.* **1979**, *34*, 249–251.

(45) Back, T. C.; Schmid, A. K.; Fairchild, S. B.; Boeckl, J. J.; Cahay, M.; Derkink, F.; Chen, G.; Sayir, A. Work function characterization of directionally solidified LaB_6/VB_2 eutectic. *Ultramicroscopy* **2017**, *183*, 67 – 71.

(46) Ravi, S. K.; Sun, W.; Nandakumar, D. K.; Zhang, Y.; Tan, S. C. Optical manipulation of work function contrasts on metal thin films. *Science Advances* **2018**, *4*, 1–8.

(47) Ford, W. E.; Gao, D.; Knorr, N.; Wirtz, R.; Scholz, F.; Karipidou, Z.; Ogasawara, K.; Rosselli, S.; Rodin, V.; Nelles, G.; von Wrochem, F. Organic Dipole Layers for Ultralow Work Function Electrodes. *ACS Nano* **2014**, *8*, 9173–9180.

(48) Baskin, A.; Lo, W.-Y.; Král, P. Clusters and Lattices of Particles Stabilized by Dipolar Coupling. *ACS Nano* **2012**, *6*, 6083–6090.

(49) Rusu, P. C.; Brocks, G. Surface Dipoles and Work Functions of Alkylthiolates and Fluorinated Alkylthiolates on Au(111). *J. Phys. Chem. B* **2006**, *110*, 22628–22634.

(50) Richardson, O. W. Some Applications of the Electron Theory of Matter. *Phil. Mag.* **1912**, *23*, 594.

(51) Dushman, S. Electron Emission from Metals as a Function of Temperature. *Phys. Rev.* **1923**, *21*, 623.

(52) Haase, J. R.; Go, D. B. Analysis of thermionic and thermo-field emission in microscale gas discharges. *J. Phys. D: Appl. Phys.* **2016**, *49*, 055206.

(53) Simon, A. H. In *Handbook of Thin Film Deposition (Third Edition)*, third edition ed.; Seshan, K., Ed.; William Andrew Publishing: Oxford, 2012; pp 55–88.

(54) Wasa, K. In *Handbook of Sputtering Technology (Second Edition)*, second edition ed.; Wasa, K., Kanno, I., Kotera, H., Eds.; William Andrew Publishing: Oxford, 2012; pp 41–75.

(55) Blank, P.; Wittmaack, K. Energy and fluence dependence of the sputtering yield of silicon bombarded with argon and xenon. *Journal of Applied Physics* **1979**, *50*, 1519–1528.

(56) Yamamura, Y.; Tawara, H. Energy dependence of ion-induced sputtering yields from monatomic solids at normal incidence. *Atomic Data and Nuclear Data Tables* **1996**, *62*, 149–253.

(57) Brown, P. R.; Lunt, R. R.; Zhao, N.; Osedach, T. P.; Wanger, D. D.; Chang, L.-Y.; Bawendi, M. G.; Bulović, V. Improved Current Extraction from ZnO/PbS Quantum Dot Heterojunction Photovoltaics Using a MoO_3 Interfacial Layer. *Nano Lett.* **2011**, *11*, 2955–2961.

(58) Lou, X. W.; Deng, D.; Lee, J. Y.; Feng, J.; Archer, L. A. Self-Supported Formation of Needlelike Co_3O_4 Nanotubes and Their Application as Lithium-Ion Battery Electrodes. *Adv. Mater.* **2008**, *20*, 258–262.

(59) Norton, J. J. S. et al. Soft, curved electrode systems capable of integration on the auricle as a persistent brain–computer interface. *PNAS* **2015**, *112*, 3920–3925.

(60) Jeong, J. W.; Shin, G.; Park, S. I.; Yu, K. J.; Xu, L.; Rogers, J. A. Soft materials in neuroengineering for hard problems in neuroscience. *Neuron* **2015**, *86*, 75–86.

(61) Comsol Multiphysics v.5.4., COMSOL AB, Stockholm, Sweden. 2018; `www.comsol.com`.

(62) Bouchoule, A.; Plain, A.; Boufendi, L.; Blondeau, J. P.; Laure, C. Particle generation and behavior in a silane-argon low-pressure discharge under continuous or pulsed radio-frequency excitation. *J. Appl. Phys.* **1991**, *70*, 1991–2000.

TOC Graphic

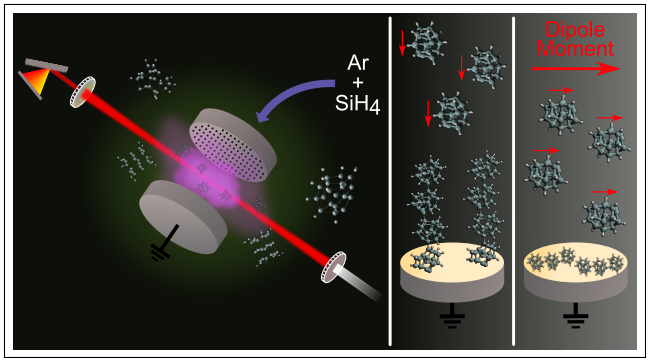

Schematic of the experimental setup for the functionalization of cathodes. Electrically neutral and ultrastable silicon clusters spontaneously formed in a plasma are analysed within an optical cavity using a supercontinuum light source. Electric fields are then used to orient and guide those individual clusters for a one-by-one surface deposition; typical behavior is illustrated on the right for two orthogonal electric fields applied during deposition.